

Comparison of weak lensing masses and X-ray properties of galaxy clusters^{*}

Henk Hoekstra

Department of Physics and Astronomy, University of Victoria, Victoria, BC, V8P 5C2, Canada

Accepted. Received; in original form

ABSTRACT

We present measurements of the masses of 20 X-ray luminous clusters of galaxies at intermediate redshifts, determined from a weak lensing analysis of deep archival R -band data obtained using the Canada-France-Hawaii-Telescope. Compared to previous work, our analysis accounts for a number of effects that are typically ignored, but can lead to small biases, or incorrect error estimates. We derive masses that are essentially model independent and find that they agree well with measurements of the velocity dispersion of cluster galaxies and with the results of X-ray studies. Assuming a power law between the lensing mass and the X-ray temperature, $M_{2500} \propto T^\alpha$, we find a best fit slope of $\alpha = 1.34^{+0.30}_{-0.28}$. This slope agrees with self-similar cluster models and studies based on X-ray data alone. For a cluster with a temperature of $kT = 5$ keV we obtain a mass $M_{2500} = (1.4 \pm 0.2) \times 10^{14} h^{-1} M_\odot$ in fair agreement with recent Chandra and XMM studies.

Key words: cosmology: observations – dark matter – gravitational lensing – galaxies: clusters

1 INTRODUCTION

Clusters of galaxies have been the focus of intense study for many decades for a variety of reasons. They are the largest gravitationally bound objects in the universe and provide a large reservoir of baryons, mainly in the form of the hot intracluster (ICM) gas. The study of galaxy clusters has been transformed recently with the advent of powerful X-ray telescopes such as Chandra and XMM, which enable us to determine the properties of the gas in unprecedented detail and accuracy. Such studies will hopefully lead to a better understanding of the complex physics of the ICM and its interaction with the various constituents of the cluster (e.g., dark matter, galaxies). The dynamical state of the ICM might also reveal information about the recent merger history, thus providing an interesting way to test the concept of hierarchical cluster formation, as predicted in the cold dark matter (CDM) paradigm.

As the most massive objects in the universe, galaxy clusters are readily found out to large redshifts in optical, X-ray or millimeter (Sunyaev-Zel'dovich; SZ) surveys. This makes them excellent cosmological probes, because the number of

clusters as a function of mass is very sensitive to a range of cosmological parameters, such as the matter density, the normalisation of the matter power spectrum and the equation of state of the dark energy (e.g., Evrard 1989; Eke et al. 1998; Henry 2000; Haiman et al. 2001; Levine et al. 2002; Allen et al. 2004). These constraints are complimentary to measurements of large scale structure and the cosmic microwave background.

Given the great interest in the use of galaxy clusters as a cosmological probe, and the advent of efficient SZ telescopes in the coming years it is important to derive accurate masses for these systems. To estimate masses from the motion of cluster galaxies, one needs to make assumptions about the orbital structure and the geometry of the cluster in addition to the assumption of equilibrium. Similarly, X-ray and SZ measurements of the total mass assume the cluster is in hydrostatic equilibrium. These assumptions are not always valid, thus complicating systematic studies of cluster properties. Finally, it is becoming increasingly clear that non-gravitational physics complicates matters further.

Fortunately, there exists a direct way to determine the cluster mass. The gradient in the gravitational potential of the cluster causes differential deflection of light rays coming from distant galaxies. This causes small, systematic distortions in the shapes of these faint sources, an effect known as weak gravitational lensing. The amplitude of the signal provides a direct measurement of the projected mass *along*

^{*} Based on observations from the Canada-France-Hawaii Telescope, which is operated by the National Research Council of Canada, le Centre National de la Recherche Scientifique and the University of Hawaii.

Table 1. Summary of the observational data for the cluster sample

name	RA	DEC	z	$t_{\text{exp}}(B)$ [s]	seeing(B) [arcsec]	$t_{\text{exp}}(R)$ [s]	seeing(R) [arcsec]
A2390	21 ^h 53 ^m 36.8 ^s	+17°41′44″	0.2280	8100	0.90	9600	0.66
MS 0016+16	00 ^h 18 ^m 33.5 ^s	+16°26′16″	0.5465	6180	0.87	9423	0.68
MS 0906+11	09 ^h 09 ^m 12.6 ^s	+10°58′28″	0.1704	6000	0.93	13800	0.84
MS 1224+20	12 ^h 27 ^m 13.5 ^s	+19°50′56″	0.3255	8640	1.01	11400	0.86
MS 1231+15	12 ^h 33 ^m 55.4 ^s	+15°25′58″	0.2353	3900	0.90	9000	0.71
MS 1358+62	13 ^h 59 ^m 50.6 ^s	+62°31′05″	0.3290	11880	1.04	6300	0.82
MS 1455+22	14 ^h 57 ^m 15.1 ^s	+22°20′35″	0.2568	4800	1.03	9000	0.67
MS 1512+36	15 ^h 14 ^m 22.5 ^s	+36°36′21″	0.3727	12540	0.90	9900	0.71
MS 1621+26	16 ^h 23 ^m 35.5 ^s	+26°34′14″	0.4275	15300	0.99	11520	0.72
A68	00 ^h 37 ^m 06.9 ^s	+09°09′24″	0.255	8100	1.05	7200	0.67
A209	01 ^h 31 ^m 52.5 ^s	−13°36′40″	0.206	7200	0.98	5400	0.70
A267	01 ^h 52 ^m 42.0 ^s	+01°00′26″	0.230	3000	0.93	4800	0.72
A383	02 ^h 48 ^m 03.4 ^s	−03°31′44″	0.187	7200	0.93	4800	0.90
A963	10 ^h 17 ^m 03.8 ^s	−39°02′51″	0.206	7200	0.88	4800	0.77
A1689	13 ^h 11 ^m 30.0 ^s	−01°20′30″	0.1832	3600	0.88	3000	0.81
A1763	13 ^h 35 ^m 20.1 ^s	+41°00′04″	0.223	3600	0.94	6000	0.85
A2218	16 ^h 35 ^m 48.8 ^s	+66°12′51″	0.1756	3378	1.06	3300	0.84
A2219	16 ^h 40 ^m 19.9 ^s	+46°42′41″	0.2256	5400	0.91	6300	0.78
A370	02 ^h 39 ^m 52.7 ^s	−01°34′18″	0.375	10408	0.92	10800	0.77
CL0024+16	00 ^h 26 ^m 35.6 ^s	+17°09′44″	0.390	12960	0.98	9000	0.64

Column 1: cluster name; Column 2,3: right ascension and declination (J2000.0) of the brightest cluster galaxy. Note that in the case of two dominant central galaxies this might differ from previous positions; Column 4: cluster redshift; Column 5,7: exposure times in the *B* and *R*-band resp.; Column 6,8: seeing in *B* and *R* resp. The top 9 clusters have been studied as part of the CNOC cluster survey. The next 9 systems are a subset of the systems studied by Bardeau et al. (2005) (although we note that A2390 is also part of that study). The last two clusters are well known clusters because of their spectacular strong lensing.

the *line of sight* in a given aperture, which in turn can be compared directly to numerical simulations, a crucial step if one wants to use clusters for cosmology. However, to compare the weak lensing results to other mass indicators one typically has to make assumptions regarding the cluster geometry.

Weak lensing is now a well established technique to study the distribution of (dark) matter in the universe and the applications are numerous (e.g., see Hoekstra et al., 2002a; Schneider 2005). In particular, recent progress in the measurement of the lensing signal caused by large scale structure (cosmic shear) has demonstrated the reliability with which the tiny distortions in the images of faint galaxies can be measured (e.g., Hoekstra et al. 2002b; Van Waerbeke et al. 2005; Hoekstra et al. 2006).

Although the first succesful detection of weak lensing was made studying a galaxy cluster (Tyson, Wenk & Valdes 1990), the sample of clusters with accurate mass determinations is relatively small. Early results are based on inhomogeneous data sets which cover only the central regions (e.g., Fahlman et al. 1994; Hoekstra et al. 1998; Squires et al. 1996a, 1996b). More recently, Dahle et al. (2002) and Cypriano et al. (2005) published results on larger samples. This situation has limited detailed comparisons of masses inferred from X-ray observations and those of lensing, although some attempts have been made (e.g., Allen 1998).

In recent years it has become possible to study the mass

distribution of clusters in much more detail, thanks to the advent of wide field imagers. These instruments enable us to measure the lensing signal out to much larger radii, improving the reliability of the results. In addition, thanks to studies of photometric redshifts for the faint galaxies used in weak lensing analysis, we can now better relate the observed lensing signal to an estimate of the cluster mass.

In this paper we present measurements of the weak lensing masses for a sample of 20 X-ray luminous clusters of galaxies observed with the CFH12k camera on the Canada-France-Hawaii Telescope (CFHT). The data used here consist of archival *B* and *R* band images, where the latter data are used in the weak lensing analysis.

The structure of the paper is as follows. In §2 we present the data and discuss the image processing. §3 deals with the weak lensing shape measurements and interpretation of the results. The mass measurements are presented in §4. In this section we also compare our results to those obtained from other techniques. Throughout the paper we assume a cosmology with $\Omega_m = 0.3$, $\Omega_\Lambda = 0.7$ and $H_0 = 100h$ km/s/Mpc.

2 DATA

We searched the CFHT archive at the Canadian Astronomical Data Centre (CADC) to find galaxy clusters that have

deep exposures in both the B and the R -band obtained using the CFH12k camera. This camera consists of an array of 6 by 2 CCDs, each 2048 by 4096 pixels. The pixel scale is $0''.206$, which ensures good sampling for the subarcsecond imaging data used here. The resulting field of view is about 42 by 28 arcminutes, significantly larger than the $\sim 8 \times 8$ arcminutes typically used in older lensing studies.

This search yielded a sample of 20 X-ray luminous clusters for which useful data could be retrieved. Nine of the clusters were observed as part of a follow-up project (PI: P. Fischer) to image the clusters studied in the Canadian Network for Observational Cosmology Cluster Redshift Survey (CNOC1; e.g., Yee et al., 1996; Carlberg et al., 1996). The latter survey is a multi-object spectroscopy survey of galaxies in moderately rich to rich clusters at intermediate redshifts ($0.17 < z < 0.55$) selected from the Einstein Medium Sensitivity Survey (EMSS; Gioia et al., 1990). Another 9 clusters in our sample were taken for another project aiming to determine weak lensing masses (PIs: Kneib, Czoske). See Bardeau et al (2005) and Smith et al. (2005) for a discussion of the $z = 0.2$ cluster sample, which is selected from the X-ray Brightest Abell Clusters Survey (XBACS; Ebeling et al., 1996). Abell 1835 is not studied here because of the lack of deep B -band imaging data. Also note that Abell 2390 is part of both samples. Finally, two additional clusters at somewhat higher redshifts are included. These clusters have been studied because of their exceptional strong lensing properties, and therefore may be considered “lensing-selected”.

Table 1 lists the total integration times in the B and R band for the selected exposures, as well as the seeing measured from the stacked images. Because the weak lensing analysis requires good image quality, we omitted poor seeing images when combining the data. We only use the R band data for the lensing analysis. The B band data are used to select cluster galaxies, and consequently we do not require excellent seeing for the B band data. The image quality of the R band data is excellent for most of the images.

2.1 Image processing

Detrended data (de-biased and flatfielded) are provided to the community through CADC. The detrending is done using the Elixir pipeline developed at CFHT. The pipeline also provides photometric zeropoints and in most cases a reasonable first order astrometric solution.

For the weak lensing analysis we use a stack of the individual exposures. This requires that the astrometry of the images be very precise. If this were not the case, the misalignment of images would introduce a spurious signal. Related to this is the need to remove the distortion of the camera, which places requirements on the overall astrometry, which are readily met using the procedure outlined below.

In principle one could use the USNO-A2 catalog to refine the astrometry, but the number density of sources is often too low to warrant stable results. Instead, we retrieve red images from the second generation Digital Sky Survey (POSS II) for each cluster. These observations have small geometric distortions. This can be taken care of by calibrating the astrometry of the POSS II images using the USNO-A2 catalog. SExtractor (Bertin & Arnouts 1996) is used to generate a catalog of sources with accurate astrometry, with a

number density significantly higher than the USNO-A2 catalog. In addition, the POSS II images have been taken more recently, thus reducing the effects of proper motions of the stars.

This new astrometric catalog is matched to each of the CFH12k exposures. We combine the matched catalogs for each exposure into a master catalog, which contains the average positions of the matched objects. This master catalog is used to derive the final second order astrometric solution for each chip. This procedure ensures that in the overlapping areas the objects are accurately matched to the same position.

The images with the improved astrometry are stacked using the SWarp routine into a large mosaic image. As discussed below, for certain regions, data from different chips contribute to the image. If the PSF properties are discontinuous between chips, this may result in complicated behaviour of the PSF. Fortunately, for most of the data, the offsets between exposures are small. In addition, the CFH12k PSF shows no evidence of “jumps”, because the chips are very well aligned (e.g., see Hoekstra et al. 2002b).

As mentioned earlier, the Elixir processed images contain photometric calibrations based on observations of standard stars during the observing run. These zero-points are only valid under photometric conditions, a condition that needs to be checked for each exposure. We therefore examine the magnitudes of a large number of objects in the images, which enables us to examine the variation in the photometric zero-point. We found that most data were taken under photometric conditions. For a few clusters only part of the data were photometric and we use these images to scale the non-photometric data.

As additional checks we compared galaxy counts (with the cluster region excised) to those provided by P. Hsieh (private communication), and the expected distribution of $B-R$ colors of stars. In both cases we found good agreement between our data and the reference data. Where available we also compared our magnitudes to those observed by the Sloan Digital Sky Survey, and found excellent agreement. As a final check, we note that colors of the cluster red-sequence are in good agreement with the expected values (the scatter around the mean is 0.03 in $B-R$).

3 WEAK LENSING ANALYSIS

In this section we discuss the details of the weak lensing analysis and how we interpret the resulting lensing signal. In §3.1 we discuss how we measure the shapes of galaxies used in the weak lensing analysis. A useful way of quantifying the lensing signal is presented in §3.2. There are various ways to estimate the cluster mass from the observed lensing signal. For instance, one can adopt a parameterized model for the density profile and fit this to the observations. We consider two such models. The singular isothermal sphere is discussed in §3.3 and the cold dark matter NFW profile (Navarro, Frenk & White 1997; NFW hereafter) is presented in §3.4. Another approach is to determine the projected mass within an aperture of a given radius, with a minimal dependence on the density profile at large radii. This approach is discussed in §3.5.

Various effects that complicate a simple interpretation

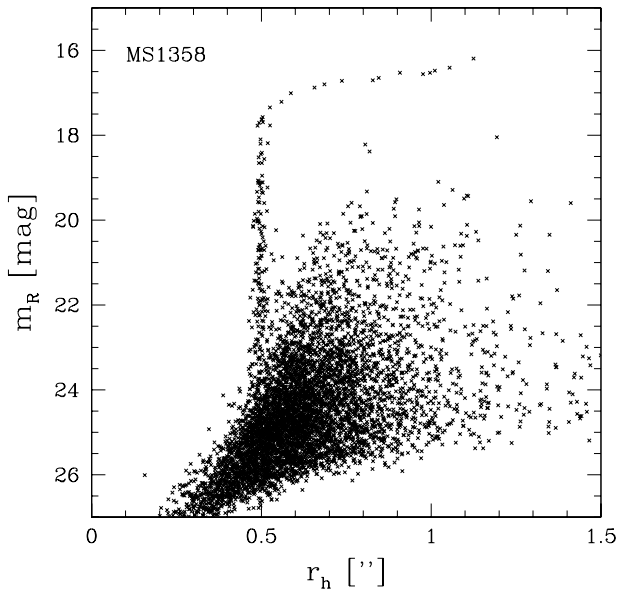


Figure 1. Plot of the apparent magnitude as a function of the measured half-light radius for the data for MS 1358. The clear vertical locus of stars at a half-light radius of ~ 0.5 allows for a clean selection of stars used to characterize the PSF.

of the lensing signal are reviewed in §3.6. In section §3.7 we discuss the contamination of the lensing signal by cluster members, which are included in the catalog of source galaxies. The conversion of the lensing signal into a mass requires knowledge of the redshift distribution of the source galaxies, which is addressed in §3.8. Finally, lensing is sensitive to all matter along the line of sight, which needs to be accounted for. This is reviewed in §3.9.

3.1 Shape measurements

The various steps in the weak lensing analysis have been described in detail in Hoekstra et al. (1998, 2000). Our method is based on the original procedure developed by Kaiser, Squires & Broadhurst (1995) and Luppino & Kaiser (1997) with modification presented by Hoekstra et al. (1998). The key step in the lensing analysis is to accurately measure the shapes of the faint background galaxies, correcting for the various observational distortions, such as seeing and PSF anisotropy.

For the weak lensing analysis we only use the stacked R -band images. As can be seen from Table 1 the R exposures have better image quality than the B -band data. Good image quality is crucial for an accurate measurement of the mass using weak lensing.

Although the PSF anisotropy varies coherently over the total field of view, we follow van Waerbeke et al. (2005) and split the coadded images into subsets which correspond approximately to the original chips. This enables us to better characterize the spatial variation of the PSF anisotropy. The various images used to obtain the deep coadded images have been taken with (typically) small offsets, which in principle complicates the analysis. However, discontinuities

in the PSF anisotropy between chips are small and can be neglected in our analysis. This is supported by the results from the VIRMOS-DESCART survey (van Waerbeke et al. 2005). These cosmic shear measurements are very sensitive to residual systematics, but do not show a significant systematic signal due to the adopted approach. We conclude by noting that the weak lensing analysis of galaxy clusters is less sensitive to residual systematics compared to cosmic shear studies.

The first step in the lensing analysis is the identification of the faint galaxies in the images. For that we use the hierarchical peak finding algorithm from Kaiser et al. (1995) to find objects with a significance $> 5\sigma$ over the local sky. The peak finder gives fair estimates for the object size, and we reject all objects smaller than the size of the PSF.

The objects in this cleaned catalog are analysed, which yields estimates for the size, apparent magnitude and shape parameters (polarisation and polarisabilities) and their measurement errors. The objects in this catalog are inspected by eye, in order to remove spurious detections. These objects have to be removed because their shape measurements are affected by cosmetic defects (such as bleeding stars, diffraction spikes from bright stars) or because the objects are likely to be part of a resolved galaxy (e.g., an HII region).

To measure the small, lensing induced distortions it is important to accurately correct the shapes for PSF anisotropy, as well as for the diluting effect of seeing. To characterize the spatial variation of the PSF we select a sample of moderately bright stars from our images. The stars are selected based on their location in a plot of the apparent magnitude as a function of half-light radius, such as the one presented in Figure 1. The stars are defined by the vertical locus at $r_h = 0.5$, and allow for a clean sample of stars. We fit a second order polynomial to the shape parameters of the selected stars for each chip, which provides us with an estimate of the PSF anisotropy at every position. These results are used to correct the shapes of the galaxies for PSF anisotropy.

Seeing circularizes the images, thus lowering the raw lensing signal. To correct for the seeing, we need to rescale the polarisations to their “pre-seeing” value. This scale factor is the “pre-seeing” shear polarisability P^γ (Luppino & Kaiser 1997; Hoekstra et al. 1998). The measurements of P^γ for each individual galaxy are noisy, and we therefore bin the measurements as a function of galaxy size, and use the ensemble average value as a function of size to correct for the effect of seeing. This approach has been tested on simulated images in great detail (e.g., Hoekstra et al. 1998; Heymans et al. 2005). These results suggest that we can recover the shear with an accuracy of $\sim 2\%$ (Heymans et al. 2005).

Having corrected the shapes of the galaxies in each “chip”, we combine the catalogs into a master catalog, which covers the full field of view. This catalog is used for the weak lensing analysis.

3.2 Tangential distortion

The azimuthally averaged tangential shear $\langle \gamma_t \rangle$ as a function of radius from the cluster centre is a useful measure of the lensing signal (e.g., Miralda-Escudé 1991):

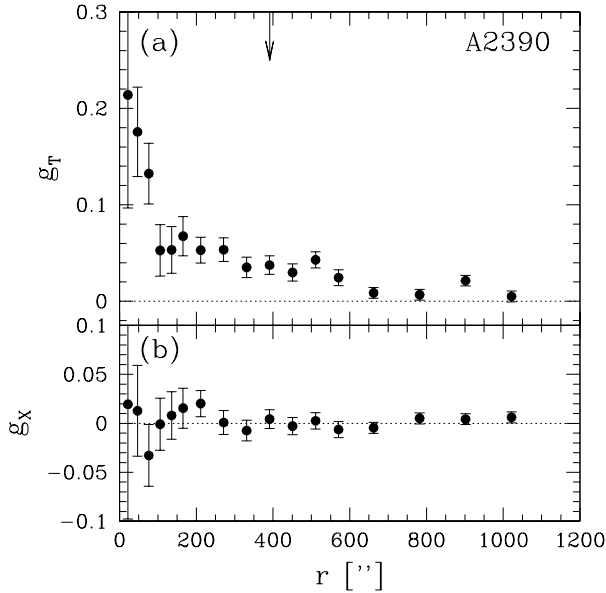


Figure 2. *Panel (a):* plot of the tangential distortion as a function of the distance from the cluster center for Abell 2390 using galaxies with $21 < R < 25$. A significant signal is measured out to large radii. The arrow indicates a radius of $1h^{-1}$ Mpc at the redshift of the cluster. *Panel (b):* the signal when the sources are rotated by 45 degrees. If the signal presented in panel a is caused by lensing, no signal should be present, as is the case. This test is similar to the “B”-modes in cosmic shear surveys.

$$\langle \gamma_t \rangle(r) = \frac{\bar{\Sigma}(< r) - \bar{\Sigma}(r)}{\Sigma_{\text{crit}}} = \bar{\kappa}(< r) - \bar{\kappa}(r), \quad (1)$$

where $\bar{\Sigma}(< r)$ is the mean surface density within an aperture of radius r , and $\bar{\Sigma}(r)$ is the mean surface density on a circle of radius r . The convergence κ , or dimensionless surface density, is the ratio of the surface density and the critical surface density Σ_{crit} , which is given by

$$\Sigma_{\text{crit}} = \frac{c^2}{4\pi G} \frac{D_s}{D_l D_{ls}}, \quad (2)$$

where D_l is the angular diameter to the lens. D_s and D_{ls} are the angular diameter distances from the observer to the source and from the lens to the source, respectively. The parameter $\beta = D_{ls}/D_s$ is a measure of how the amplitude of the lensing signal depends on the redshifts of the source galaxies.

Figure 2a shows the observed lensing signal as a function of distance from the cluster center for Abell 2390. The center is taken to be the position of the brightest cluster galaxy. A significant signal is measured out to large radii. Panel b indicates a test for systematics: if the signal presented in panel a is caused by lensing, no signal should be present, as is observed. To minimize the contamination by cluster members, we have excluded galaxies with colors similar to the cluster color-magnitude relation (see §3.7 for a more detailed discussion).

3.3 Singular Isothermal Sphere

A simple model for the cluster mass distribution is the singular isothermal sphere (SIS) for which the convergence and tangential shear are given by

$$\kappa = \langle \gamma_t \rangle = \frac{r_E}{2r}, \quad (3)$$

where r_E is the Einstein radius. For the clusters in our sample we fit this model to the observed lensing signal (taking into account the complicating factors discussed below) from 0.25 to $1h^{-1}$ Mpc, and the resulting values with their statistical errors are listed in Table 2.

Under the assumption of isotropic orbits and spherical symmetry, the Einstein radius (in radians) is related to the line-of-sight velocity dispersion through

$$r_E = 4\pi \left(\frac{\sigma}{c} \right)^2 \beta, \quad (4)$$

which allows for a direct comparison with measurements of the line-of-sight velocity dispersion of cluster galaxies from redshift surveys. We compare our lensing results with these dynamical measurements in §4.2.

3.4 NFW profile

Collisionless cold dark matter (CDM) provides a good description for the observed structure in the universe. Numerical simulations, indicate that on large scales CDM gives rise to a particular density profile (e.g., Dubinski & Carlberg 1991; Navarro, Frenk, & White 1995; Navarro, Frenk, & White 1997; Moore et al. 1999). In these simulations, the NFW profile, given by

$$\rho(r) = \frac{M_{\text{vir}}}{4\pi f(c)} \frac{1}{r(r+r_s)^2}, \quad (5)$$

appears to be an good description of the radial mass distribution for halos with a wide range in mass. Here, M_{vir} is the virial mass, which is the mass enclosed within the radius r_{vir} . The virial radius is related to the scale radius through the concentration $c = r_{\text{vir}}/r_s$, and the function $f(c) = \ln(1+c) - c/(1+c)$.

One can fit the NFW profile to the measurements with M_{vir} and concentration c (or equivalently r_s) as free parameters. However, numerical simulations have shown that the average concentration depends on the halo mass and the redshift (Bullock et al. 2001)

$$c = \frac{9}{1+z} \left(\frac{M_{\text{vir}}}{8.12 \times 10^{12} h M_{\odot}} \right)^{-0.14}. \quad (6)$$

For the NFW mass estimates presented in §4, we will use this relation between mass and concentration, thus assuming we can describe the cluster mass distribution with a single parameter. We note that the simulations show considerable scatter in the profiles from halo to halo. For instance, the values of c for halos of a given mass have a lognormal dispersion of approximately 0.14 around the median.

By definition, the virial mass and radius are related through

$$M_{\text{vir}} = \frac{4\pi}{3} \Delta_{\text{vir}}(z) \rho_{\text{bg}}(z) r_{\text{vir}}^3, \quad (7)$$

Table 2. Results for the singular isothermal sphere model

(1) name	(2) R_C [mag]	(3) $\langle\beta\rangle$	(4) $\langle\beta^2\rangle$	(5) D_l [h^{-1} Gpc]	(6) $1h^{-1}$ Mpc ["]	(7) r_E ["]	(8) σ_{r_E} ["]	(9) σ_{LSS} ["]	(10) σ_{tot} ["]
A2390	21-25	0.54	0.34	0.53	391	19.4	2.3	1.3	2.6
MS 0016+16	22-25.5	0.24	0.11	0.92	223	9.2	2.2	1.0	2.4
MS 0906+11	21-25	0.62	0.43	0.42	492	13.9	2.7	1.6	3.2
MS 1224+20	21-25	0.40	0.21	0.68	303	8.1	2.4	1.1	2.7
MS 1231+15	21-25.5	0.54	0.35	0.54	382	5.0	2.3	1.5	2.8
MS 1358+62	21-25	0.40	0.22	0.69	301	12.6	2.2	1.1	2.5
MS 1455+22	21-25.5	0.52	0.33	0.58	358	13.9	2.1	1.4	2.5
MS 1512+36	22-25.5	0.40	0.22	0.74	278	5.9	2.2	1.2	2.5
MS 1621+26	22-25.5	0.34	0.18	0.81	255	9.7	2.3	1.1	2.5
A68	21-25	0.49	0.29	0.57	360	15.2	2.3	1.3	2.6
A209	21-25	0.57	0.38	0.49	423	13.3	2.3	1.4	2.7
A267	20-25	0.53	0.33	0.53	389	15.5	2.4	1.3	2.8
A383	21-24.5	0.58	0.38	0.45	456	8.2	3.2	1.3	3.4
A963	21-25	0.57	0.37	0.49	423	11.6	2.4	1.4	2.8
A1689	21-24.5	0.60	0.40	0.44	464	32.2	2.7	1.3	2.9
A1763	21-25	0.54	0.33	0.52	398	17.3	2.5	1.4	2.9
A2218	21-24.5	0.61	0.42	0.43	480	19.1	2.9	1.3	3.2
A2219	21-25	0.54	0.34	0.52	394	17.9	2.4	1.4	2.7
A370	22-25	0.37	0.19	0.75	277	19.7	2.4	1.0	2.6
CL0024+16	22-25.5	0.36	0.19	0.76	270	13.6	2.4	1.2	2.7

Column 1: cluster name; Column 2: adopted range in apparent magnitude for the source galaxies; Column 3: effective value of $\langle\beta\rangle$ as described in the text. The derived statistical error is 0.01; Column 4: value for $\langle\beta^2\rangle$; Column 5: angular diameter distance to the cluster; Column 6: angular size corresponding to $1h^{-1}$ Mpc; Column 7: value for the Einstein radius r_E obtained from a SIS model fit to the tangential distortion from 0.25 to $1.5 h^{-1}$ Mpc; Column 8: statistical error for the measurement of the Einstein radius; Column 9: uncertainty in r_E caused by uncorrelated large scale structure along the line of sight; Column 10: total uncertainty in r_E , combining the statistical and LSS errors.

where $\rho_{\text{bg}} = 3H_0^2\Omega_m(1+z)^3/(8\pi G)$ is the mean density at the cluster redshift and the virial overdensity $\Delta_{\text{vir}} \approx (18\pi^2 + 82\xi - 39\xi^2)/\Omega(z)$, with $\xi = \Omega(z) - 1$ (Bryan & Norman 1998). For the Λ CDM cosmology considered here, $\Delta_{\text{vir}}(0) = 337$.

Cluster masses are also often quoted in terms of M_Δ , which is the mass contained within the radius r_Δ , where the mean mass density of the halo is equal to Δ times the critical density at the redshift of the cluster. For reference with other work, we list results for a number of commonly used values for Δ . Note that M_{200} is often referred to as the virial mass, but that our definition for M_{vir} is different.

The expressions for the tangential shear and surface density for the NFW profile have been derived by Bartelmann (1996) and Wright & Brainerd (2000) and we refer the interested reader to these papers for the relevant equations.

3.5 Aperture mass

Another approach to determine the cluster mass is known as aperture mass densitometry. It uses the fact that the shear can be related directly to a density contrast. We use the statistic of Clowe et al (1998), which is related to the ζ -statistic of Fahlman et al. (1994).

In terms of the dimensionless surface density $\zeta_c(r_1)$ is equal to the mean surface density interior to r_1 relative to the mean surface density in an annulus from r_2 to r_{max}

$$\zeta_c(r_1) = \bar{\kappa}(r' < r_1) - \bar{\kappa}(r_2 < r' < r_{\text{max}}). \quad (8)$$

It is related to the (observed) shear through

$$\zeta_c(r_1) = 2 \int_{r_1}^{r_2} d \ln r \langle \gamma_t \rangle + \frac{2r_{\text{max}}^2}{r_{\text{max}}^2 - r_2^2} \int_{r_2}^{r_{\text{max}}} d \ln r \langle \gamma_t \rangle. \quad (9)$$

Equation 8 shows that we can determine the average surface density within a given aperture up to a constant. If we ignore the surface density in the annulus, ζ_c provides a lower limit to the mass. This demonstrates the usefulness of wide field imaging data: at large radii, the mean surface density in the annulus should be small and its contribution relative to the mean surface density within r_1 decreases.

We use the surface density from the NFW model to convert the observed signal into an estimate of the shear. In this case the mass estimate is based on the signal measured at large radii, and the correction is small.

For the mass estimates presented in §4, we adopt $r_2 = 600''$ and $r_{\text{max}} = 1000''$. We estimate the mean surface density in the annulus based on the best fit NFW model. Thanks to our ability to measure the lensing signal out to large radii, the (model dependent) correction to the mass is only $\sim 10\%$.

3.6 Complications in weak lensing mass estimates

Hoekstra et al. (2000) lists various effects which complicate a simple interpretation of the lensing signal. Some of these

have typically been included in published weak lensing studies, but others are often ignored. We therefore briefly review them here.

First of all, the observed lensing signal is invariant under the transformation $\kappa' = (1 - \lambda)\kappa + \lambda$, which is usually referred to as the mass sheet degeneracy (Gorenstein, Shapiro & Falco 1988): we can determine the surface density up to a constant. This can also be seen from Eqn. 8, where one needs to estimate the mean surface density in an annulus to derive the enclosed mass. At very large radii, however, the cluster surface density should be small, and the mass sheet degeneracy is less relevant. As mentioned above, we estimate the mass in the annulus from a mass model, and find that the correction to the enclosed mass is typically less than 10%. Hence, the uncertainty in the mass due to the mass sheet degeneracy is a few percent at most for the wide field imaging data used here.

The images of the distant galaxies are not only distorted, but also magnified. The flux is increased by a factor $\mu = ((1 - \kappa)^2 - \gamma^2)^{-1}$. This changes the source redshift distribution as intrinsically fainter galaxies are included as sources. This effect is small, even in the inner regions of the cluster where the surface density is large. It is therefore safe to ignore this effect in our analysis.

A complication which is relevant for our measurements, is the fact that we do not measure the shear γ from the data, but the distortion (or reduced shear) $g = \gamma/(1 - \kappa)$. In the weak lensing limit ($\kappa \ll 1$), the distortion is equal to the shear, but even at the large radii probed here, the amplitude of this effect is a few percent. Hence, it is important to account for the $(1 - \kappa)$ factor in our cluster mass estimates.

3.7 Contamination by cluster galaxies

Weak lensing observations typically lack redshift information for the galaxies used in this analysis. As a result we cannot distinguish between unlensed cluster galaxies and lensed sources. The contamination by cluster galaxies will lower the lensing signal (where we assume their orientations are random) and therefore needs to be accounted for, i.e., we need to increase the observed shear by a factor $1 + f_{cg}(r)$, where f_{cg} is the fraction of cluster galaxies at that radius. Note that foreground field galaxies also dilute the lensing signal, but this is naturally accounted for in the calculation of the critical surface density (see Eqn. 2 and the discussion in §3.8)

We used our data to examine the excess counts of galaxies as a function of distance from the cluster. We combined the measurements of the clusters in our sample. The amount of contamination at a given angular or physical scale depends on the mass (or richness) of the cluster. Although the range in mass is relatively small, we found that the profiles match best if we use the radius in units of r_{2500} (or equivalently the virial radius). Note, that this does not require a scaling of the counts themselves.

We also examined whether the contamination depends on cluster redshift. One might expect this, because the red-sequence occupies different regions in the color-magnitude diagram as a function of redshift. However, we did not find a significant trend with redshift and we therefore assume the correction is redshift independent.

The results are presented in Figure 3. The shaded area

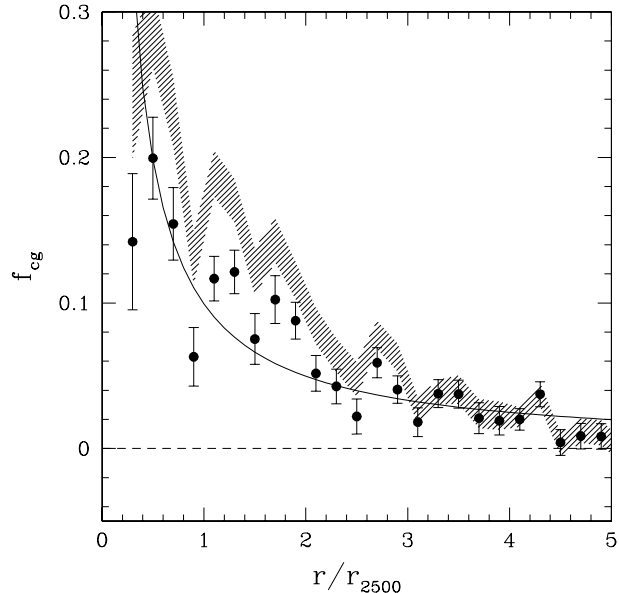


Figure 3. Fraction of cluster galaxies f_{cg} as a function of radius from the cluster center in units of r_{2500} . The points indicate the contamination after removal of galaxies with colors along the cluster red-sequence. The shaded area corresponds to the level of contamination if no color selection is applied. The level of contamination is reduced by only $\sim 30\%$ by applying a color cut. However, it is clear that some contamination remains at small radii. The solid line is the best fit $1/r$ model.

indicates the fraction of cluster galaxies as a function of radius if no color selection is used for the sources. At r_{2500} (which roughly corresponds to ~ 2 arcminutes for the clusters considered here) we find that about 14% of the galaxies are cluster members. Thanks to our color information, we can define a cluster red-sequence and reject galaxies that lie on this sequence. To do so we identify the red ridge of the cluster color-magnitude relation and select all galaxies that are up to ~ 0.3 magnitudes bluer. This removes the bright elliptical galaxies quite effectively, but at fainter magnitudes, the red-sequence is not well defined and many cluster members are actually blue. Consequently the color selection reduces the contamination by a modest $\sim 30\%$ to 10% at r_{2500} . This remaining contamination is typically ignored in the literature.

Comparison to the overdensity of red galaxies shows that the observed contamination traces the distribution of red galaxies well. At large radii the measurements are noisy and suffer from the fact that it is difficult to determine the background level. We used the counts in an annulus from 10 to 15 arcminutes (more than 5 times r_{2500} for most clusters) from the cluster centre. This may not be sufficiently far out, and as a result we may underestimate the contamination at large radii. It is clear, however, that the contamination is small at large radii.

To estimate the level of contamination as a function of radius we assume that $f_{cg} \propto r^{-1}$ (as the data do not allow a good estimate of the slope). The best fit result is indicated by the solid line in Figure 3. We use this model to correct the

tangential shear measurements for contamination by cluster members. The corrections are small, and we determine r_{2500} from the uncorrected shear profile, and use this to correct the profile and redetermine r_{2500} . This iteration scheme converges rapidly. We find that our correction for the residual contamination by cluster members increases the measured Einstein radii by $\sim 7\%$ (see Table 2). The aperture masses listed in Table 3 are affected less, and the mass within an aperture of radius of $0.5h^{-1}\text{Mpc}$ increases by $\sim 4\%$.

3.8 Source redshift distribution

As mentioned above, the interpretation of the lensing signal requires knowledge of the redshifts of the source galaxies. Based on our data alone, we do not know the redshifts of the individual sources. The observed lensing signal, however, is an ensemble average of many different galaxies, each with their own redshift. As a result, it is sufficient to know the source redshift distribution to compute $\langle\beta\rangle$.

The source galaxies are typically too faint to be included in spectroscopic redshift surveys, although much progress is expected in the coming years. Instead we use the photometric redshift distributions determined from the Hubble Deep Fields (Fernandez-Soto et al. 1999). The clusters in our sample are at relatively low redshifts, which reduces the uncertainty in the mass measurements caused by errors in the redshift distribution. The HDF redshift distribution matches redshift distributions from other (shallower) photometric redshift surveys, such as COMBO-17 (Wolf et al. 2004) and the Red-Sequence Cluster Survey (P. Hsieh private communication).

As discussed in the previous section, we identify the cluster color-magnitude relation and remove galaxies with similar colors as the cluster galaxies from the source catalogs. This increases the lensing signal in the central regions. Consequently the color cut changes the redshift distribution of the source galaxies, but we find that the effect is very small. It is negligible for the higher redshift clusters, but lowers the value for $\langle\beta\rangle$ by $\sim 2\%$ for clusters at $z \sim 0.2$.

The noise in the shape measurements for the faintest galaxies is large, which is further amplified by the large correction for seeing. We therefore limit the range in apparent magnitude for the sources used in the analysis. The adopted range is listed in Table 2. Following Hoekstra et al. (2000) we weight the shapes proportional to the inverse square of the measurement error and adjust the redshift distribution accordingly. All the considerations listed above lead to an effective value for $\langle\beta\rangle$, which is listed in Table 2. We estimate a statistical error in $\langle\beta\rangle \sim 0.01$. This value is similar for all the clusters in our sample (note, however, that the relative error is larger for the higher redshift clusters).

When computing the ensemble averaged distortion, one uses an average value of β for the sources. In doing so, one effectively assumes that the redshift distribution can be approximated by a sheet of galaxies at a redshift corresponding to the mean value of β . As shown by Hoekstra et al. (2000) this results in an overestimate of the shear by a factor

$$1 + \left[\frac{\langle\beta^2\rangle}{\langle\beta\rangle^2} - 1 \right] \kappa. \quad (10)$$

For high redshift clusters this effect can be of comparable size as the correction for the fact that we measure the

reduced shear. It is, however, typically ignored in the literature. We computed the values for $\langle\beta^2\rangle$ using the HDF photometric redshift distributions and the results are listed in Table 2. We include this correction for the mass estimates presented in §4.

3.9 Projection effects

The fact that lensing is sensitive to all matter along the line of sight complicates the direct comparison with other mass estimates. One complication is the three-dimensional structure of clusters (e.g., Corless & King, 2006). Although the measurement of the weak lensing signal does not require any assumptions about the geometry of the cluster, one does need to make such assumptions when comparing to other mass indicators, which depend on the cluster mass distribution in a different way. Therefore some of the scatter between the various mass estimates presented in §4 will be caused by this effect.

Large scale structure gives rise to two distinct contributions, both of which have been studied in detail. Structures associated with the cluster, such as filaments, have been studied by Metzler et al. (1999; 2001) using numerical simulations. Unfortunately, these studies focussed on the use of aperture mass measurements at large radii, which makes it difficult to estimate the effect for our mass model fits. Nevertheless, it is clear from Metzler et al. (2001), that the effect is significantly reduced by focussing on the central regions of the cluster, which are much denser than the cosmic web. Alternatively, provided photometric redshift of the sources are available, one can reconstruct the three-dimensional mass distribution (e.g., Taylor et al. 2004) and correct for additional structures along the line of sight.

The other contribution, arises from distant (uncorrelated) large scale structure. The observed aperture mass $M_{\text{obs}}(\theta)$ is the sum of the actual mass of the cluster $M_{\text{cl}}(\theta)$ and the contribution from all other structure along the line of sight $M_{\text{LSS}}(\theta)$. The expectation value for the latter contribution vanishes, although the distribution is slightly skewed. Therefore, on average, the distant large scale structure does not bias the lensing mass, but it introduces an additional uncertainty in the mass measurement of size $\langle M_{\text{LSS}}^2 \rangle^{1/2}$. This effect was first studied in detail in Hoekstra (2001) and Hoekstra (2003) using a semi-analytic approach which has been verified using numerical simulations by White et al. (2002).

The noise introduced by the large scale structure can be written as an integral of the projected convergence power spectrum $P_\kappa(l)$ multiplied by a filter function $g(l, \theta)$, which depends on the adopted statistic (Hoekstra 2001)

$$\langle M_{\text{LSS}}^2 \rangle(\theta) = 2\pi \int_0^\infty dl l P_\kappa(l) g(l, \theta)^2. \quad (11)$$

The expressions for $P_\kappa(l)$ and $g(l, \theta)$ can be found in Hoekstra (2001). For the purpose of this paper it suffices to note that the amplitude of the contribution of distant large scale structure depends on the adopted cosmology and source redshift distribution. For the former we adopt a ΛCDM cosmology with $\sigma_8 = 0.85$, while the source redshift distribution is the same as the one used in the cluster weak lensing analysis.

The resulting additional uncertainty in the value of the

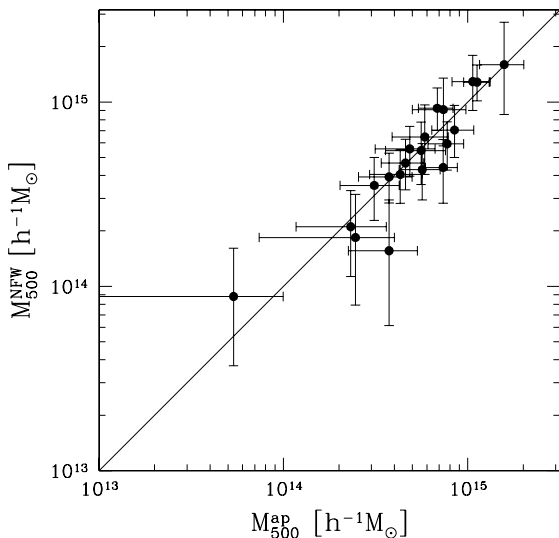


Figure 4. Comparison of M_{500} determined from an NFW fit to the data at radii $0.25 < r < 1h^{-1}$ Mpc and the value for M_{500} derived from the aperture mass method. The latter predominantly uses data at large radii, whereas the former is based on the lensing signal at small scales (note that the fitted range is smaller than for the values listed in Table 3). The two measurements are almost independent as the average r_{500} for the sample studied here is $870h^{-1}$ kpc. The solid line corresponds to the line of equality.

Einstein radius is listed in column 9 in Table 2. This additional error should be added in quadrature to the statistical error (as the two sources of uncertainty are uncorrelated), resulting in the total error listed in column 10. Including the contribution from large scale structure increases the uncertainty in the determination of the Einstein radius by 10 – 15%.

As shown in Hoekstra (2001) the effect of distant large scale is more important for aperture mass measurements, which is not surprising, given that such a mass determination depends on the lensing signal at large radii (e.g., see Eqn. 9). We find that for the aperture mass measurements, the contribution from large scale structure increases the true uncertainty by 20 – 30% over the statistical error. Similarly we follow Hoekstra (2003) to estimate the errors for the NFW model fits. We do not list the additional uncertainties separately, but note that the large scale structure contribution is included in the errors listed in Table 3.

4 MASS ESTIMATES

Table 3 lists the various weak lensing mass estimates. Column 2 shows the inferred line-of-sight velocity dispersions from the SIS model fit discussed in §3.3. These results can be compared directly to velocity dispersions of galaxies from spectroscopic observations, which is done in §4.2. The error bars include both the statistical and distant large scale structure errors.

Column 3 shows the projected mass within an aperture of $0.5h^{-1}$ Mpc using the aperture mass technique. This mea-

surement requires no assumptions about the geometry or mass profile (apart from the small correction for the mean surface density in the annulus). However, it is difficult to compare this result to other mass indicators such as X-ray properties because the latter typically assume spherical symmetry.

The virial mass as defined by Eqn. 7 is of interest, because it has some physical meaning. Given the low density in the Λ CDM model, the virial radius is rather large for the clusters considered here, and cannot be computed from the aperture mass method for two reasons. The first is that the area covered by the observations is not large enough. The second reason is more fundamental: as described in the previous section, projection effects limits the accuracy of the weak lensing mass determination. At the virial radius these errors are too large for a useful measurement.

Instead, we list the values for M_{2500} and M_{500} in Table 3, where the overdensities are measured with respect to the critical density at the redshift of the cluster. For these values of Δ we can derive reasonably accurate masses in a model independent manner. For the comparison with the ASCA data in §4.3, the M_{2500} is most relevant as r_{2500} is close to the radius out to which X-ray temperatures are measured.

We also fitted the NFW profile to the lensing signal at radii $0.25 < r < 1.5h^{-1}$ Mpc, which is the same range as was used for the SIS model fit. The resulting virial masses for this model are presented in Column 9 of Table 3. For completeness, we also list the corresponding masses for a range of other values of Δ which are commonly found in the literature (see §3.4 for details).

We can measure M_{500} in two different ways, which are almost independent. The aperture mass is predominantly based on data at large radii, whereas the NFW model fit uses measurements at small scales. The comparison of these mass estimates provides an additional check of the weak lensing analysis. We compare these two mass estimates in Figure 4, where we limited the NFW fit to radii $0.25 < r < 1h^{-1}$ Mpc, to minimize the overlap with the scales used for the aperture mass measurement (the mean value for r_{500} for the clusters in our sample is $870h^{-1}$ kpc). We find that the mass estimates agree quite well.

4.1 Comparison with published weak lensing results

Weak lensing masses have been published for a fair number of the clusters in our sample, based on observations using a wide range of telescopes and cameras. In this section we compare our results to the literature values. Before proceeding, we want to stress that in many cases the comparison is crude at best, because of differences in the assumed source redshift distribution, removal of cluster members, assumed mass model, etc.

The first detection of a weak lensing signal was presented in Tyson et al. (1991) based on the analysis of A1689. Since then, several mass estimates for this cluster have been published, and we focus on two recent ones. Based on wide field imaging data from the ESO 2.2m telescope, Clowe & Schneider (2001) estimate a velocity dispersion of $\sigma = 1162 \pm 40$ km/s (using a mean source redshift of ~ 0.5), which implies a mass which is about 30% lower than our

Table 3. Weak lensing mass estimates

(1) name	(2) σ_{WL} [km/s]	(3) $M(< 0.5h^{-1}\text{Mpc})$	(4) M_{2500}	(5) M_{500}	(6) M_{2500}^{NFW}	(7) M_{500}^{NFW}	(8) M_{200}^{NFW}	(9) $M_{\text{vir}}^{\text{NFW}}$
A2390	1117_{-82}^{+76}	5.2 ± 0.6	2.4 ± 0.5	6.8 ± 1.5	2.9 ± 0.6	$9.2_{-1.9}^{+2.0}$	$14.6_{-2.9}^{+3.1}$	$18.0_{-3.6}^{+3.8}$
MS 0016+16	1164_{-173}^{+151}	7.9 ± 1.1	3.2 ± 0.7	15.8 ± 4.3	$4.2_{-1.3}^{+1.4}$	$16.0_{-4.9}^{+5.3}$	$27.0_{-8.4}^{+9.0}$	$32.0_{-9.9}^{+10.7}$
MS 0906+11	880_{-111}^{+99}	3.7 ± 0.7	1.6 ± 0.4	7.4 ± 1.5	1.5 ± 0.4	$4.4_{-0.2}^{+1.2}$	$6.7_{-1.8}^{+1.8}$	$8.3_{-2.3}^{+2.3}$
MS 1224+20	837_{-158}^{+133}	3.0 ± 0.9	1.0 ± 0.4	2.3 ± 1.2	0.8 ± 0.4	$2.1_{-1.0}^{+1.2}$	$3.2_{-1.5}^{+1.8}$	$3.8_{-1.8}^{+2.1}$
MS 1231+15	566_{-195}^{+145}	0.8 ± 0.6	0.4 ± 0.2	0.5 ± 0.5	0.4 ± 0.2	$0.9_{-0.5}^{+0.5}$	$1.3_{-0.7}^{+0.7}$	$1.5_{-0.9}^{+0.9}$
MS 1358+62	1048_{-113}^{+102}	4.3 ± 0.8	1.8 ± 0.4	5.6 ± 2.0	$1.8_{-0.5}^{+0.6}$	$5.5_{-1.7}^{+1.9}$	$8.5_{-2.6}^{+3.0}$	$10.3_{-3.1}^{+3.6}$
MS 1455+22	964_{-95}^{+87}	3.3 ± 0.7	1.2 ± 0.3	3.7 ± 1.2	$1.4_{-0.3}^{+0.4}$	$3.9_{-1.0}^{+1.0}$	$6.0_{-1.5}^{+1.6}$	$7.3_{-1.8}^{+1.9}$
MS 1512+36	722_{-181}^{+145}	2.1 ± 0.8	0.6 ± 0.3	2.5 ± 1.6	$0.7_{-0.3}^{+0.4}$	$1.8_{-0.9}^{+1.1}$	$2.8_{-1.4}^{+1.6}$	$3.3_{-1.6}^{+1.9}$
MS 1621+26	998_{-146}^{+128}	5.3 ± 1.0	1.7 ± 0.7	5.8 ± 2.0	$2.0_{-0.6}^{+0.8}$	$6.5_{-1.9}^{+2.8}$	$10.3_{-3.0}^{+4.4}$	$12.3_{-3.6}^{+5.2}$
A68	1036_{-97}^{+89}	4.4 ± 0.8	1.9 ± 0.4	4.8 ± 1.8	$1.8_{-0.4}^{+0.5}$	$5.6_{-1.3}^{+1.6}$	$8.6_{-2.1}^{+2.5}$	$10.5_{-2.5}^{+3.1}$
A209	898_{-102}^{+92}	3.9 ± 0.9	1.5 ± 0.6	5.7 ± 1.4	$1.5_{-0.4}^{+0.5}$	$4.3_{-1.1}^{+1.4}$	$6.6_{-1.7}^{+2.1}$	$8.0_{-2.1}^{+2.5}$
A267	1008_{-99}^{+90}	3.3 ± 0.6	1.5 ± 0.3	4.3 ± 1.4	1.4 ± 0.4	$4.0_{-1.2}^{+1.2}$	$6.2_{-1.8}^{+1.9}$	$7.5_{-2.2}^{+2.3}$
A383	701_{-171}^{+138}	2.6 ± 0.7	0.6 ± 0.3	3.7 ± 1.6	$0.6_{-0.3}^{+0.4}$	$1.6_{-0.8}^{+0.9}$	$2.3_{-1.2}^{+1.3}$	$2.8_{-1.5}^{+1.6}$
A963	844_{-112}^{+99}	2.7 ± 0.6	1.0 ± 0.3	3.1 ± 1.1	1.3 ± 0.4	$3.5_{-1.0}^{+1.1}$	$5.3_{-1.5}^{+1.6}$	$6.5_{-1.9}^{+2.0}$
A1689	1370_{-68}^{+65}	6.7 ± 0.7	3.7 ± 0.5	11.2 ± 1.8	$4.0_{-0.7}^{+0.8}$	$12.8_{-2.3}^{+2.7}$	$20.4_{-3.6}^{+4.2}$	$25.5_{-4.5}^{+5.3}$
A1763	1060_{-95}^{+87}	4.9 ± 0.7	2.3 ± 0.4	8.5 ± 2.2	2.3 ± 0.6	$7.0_{-1.7}^{+2.0}$	$11.0_{-2.7}^{+3.0}$	$13.5_{-3.3}^{+3.7}$
A2218	1042_{-94}^{+87}	4.5 ± 0.7	2.0 ± 0.5	4.6 ± 1.2	$1.6_{-0.4}^{+0.5}$	$4.7_{-1.3}^{+1.5}$	$7.1_{-1.9}^{+2.3}$	$8.8_{-2.4}^{+2.8}$
A2219	1074_{-89}^{+82}	5.0 ± 0.7	2.3 ± 0.4	7.7 ± 1.7	$2.0_{-0.5}^{+0.6}$	$5.9_{-1.4}^{+1.7}$	$9.2_{-2.2}^{+2.7}$	$11.3_{-2.7}^{+3.2}$
A370	1359_{-96}^{+90}	6.5 ± 0.9	3.1 ± 0.5	10.6 ± 2.5	$3.7_{-0.9}^{+1.1}$	$12.9_{-3.2}^{+3.8}$	$21.1_{-5.3}^{+6.2}$	$25.5_{-6.4}^{+7.5}$
CL0024+16	1140_{-123}^{+111}	5.5 ± 0.9	2.3 ± 0.5	7.4 ± 2.4	$2.7_{-0.8}^{+0.9}$	$9.1_{-2.7}^{+3.2}$	$14.7_{-4.4}^{+5.1}$	$17.6_{-5.3}^{+6.2}$

Column 1: cluster name; Column 2: velocity dispersion derived from the SIS model; Column 3: projected mass enclosed in an aperture of radius $0.5h^{-1}\text{Mpc}$ in units of $10^{14}h^{-1}M_{\odot}$; Column 4,5: the mass from the aperture mass measurement. The values correspond to the mass in a sphere of radius r_{2500} and r_{500} , where the mean density is 2500 and 500 times the critical density at the redshift of the cluster, respectively; Columns 6-9: M_{2500} , M_{500} , M_{200} and the virial mass M_{vir} as derived from an NFW fit to the tangential distortion at radii $0.25 - 1.5h^{-1}\text{Mpc}$; All masses are in units of $10^{14}h^{-1}M_{\odot}$ and the error bars correspond to the 68% confidence interval. We refer the reader to §3.4 for the precise definitions of the virial mass and M_{Δ} employed in this paper.

value. The analysis presented in Clowe & Schneider (2001) lacked color information, and hence a possible explanation for the lower signal could be contamination by cluster members. The comparison with the measurement of Bardeau et al. (2005) is of particular interest because it is based on the same data used here, although the data processing and weak lensing analysis are completely independent. Bardeau et al. (2005) list an Einstein radius of 22 ± 3 arcseconds, using a fit to the lensing signal from $70''$ to $1100''$. Matching our measurement to their range, and ignoring contamination by cluster members, lowers our estimate for the Einstein radius from $32. \pm 2.6$ to 25.9 ± 1.7 arcseconds, which is still 18% higher than Bardeau et al. (2005). More recently, Limousin et al. (2006) used a combined strong and weak lensing analysis. They list a value of $M_{200} = (19 \pm 3) \times 10^{14}h^{-1}M_{\odot}$, which is in excellent agreement with our result. On small scales, however, the weak lensing analysis appears to underestimate the mass. Limousin et al. (2006) find a projected mass of $(2.7 \pm 0.4) \times 10^{14}h^{-1}M_{\odot}$ within a radius of $45''$. Extrapolating the weak lensing aperture mass measurements inwards to this small scale, we find a mass of $(2 \pm 0.3) \times 10^{14}h^{-1}M_{\odot}$.

Another well studied cluster is MS1224+20, because of its apparent high mass-to-light ratio. Fahlman et al. (1994) list a projected mass within a 2.76 radius of $3.5 \times 10^{14}h^{-1}M_{\odot}$, which is only slightly larger than our result of

$(3.0 \pm 0.6) \times 10^{14}h^{-1}M_{\odot}$. The cluster was also observed by Fischer (1999) who inferred a velocity dispersion of ~ 1300 km/s, considerably higher than our estimate. The lensing signal presented in Fischer (1999) barely decreases with distance, which is not observed in our data, and we cannot find an obvious explanation for this difference.

Squires et al. (1996a) studied A2390 and list a projected mass enclosed within a $100''$ aperture of $1.8 \times 10^{14}h^{-1}M_{\odot}$, in excellent agreement with our estimate of $2.1 \times 10^{14}h^{-1}M_{\odot}$. For A2218, Squires et al. (1996b) list a mass $M(< 3.5) = (4.6 \pm 1.4) \times 10^{14}h^{-1}M_{\odot}$, which is higher than our value of $3.4 \times 10^{14}h^{-1}M_{\odot}$.

Dahle et al. (2002) studied a sample of 38 X-ray luminous clusters, 6 of which overlap with our sample. We compared the estimates for the velocity dispersion listed in Table 2 of Dahle et al. (2002) to our results and found fair agreement for A209, A267, A963, A1763, and A2219. However, Dahle et al. (2002) list a velocity dispersion of 1650 ± 220 for A68, which is significantly higher than our measurement. Unfortunately we were unable to identify a reason for this difference.

The mass distribution of MS1358+62 was studied by Hoekstra et al. (1998) using a mosaic of WFPC2 pointings. Hoekstra et al. (2002) provide an updated value for the velocity dispersion of $\sigma = 835_{-56}^{+52}$. This number is lower than

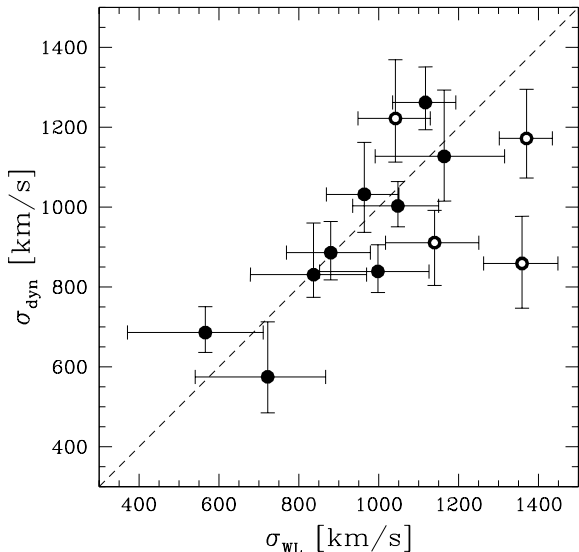


Figure 5. Plot of the velocity dispersion derived from the SIS fit to the observed tangential distortion versus the velocity dispersion of cluster galaxies from spectroscopic observations. The dashed line indicates the line of equality between the two estimates of the velocity dispersion. The large solid points are the clusters in the CNOC1 sample, and the open circles correspond to the results presented in Girardi & Mezzetti (2001).

the value of 1048^{+102}_{-113} km/s found in the CFH12k analysis, but could be due to differences in the range of scales that were fitted.

CL0024+16 was also studied using HST observations. Kneib et al. (2003) were able to probe the lensing signal out to $\sim 10'$ by sparsely covering the area with WFPC2 pointings. A direct comparison is complicated by the fact that Kneib et al. (2003) do not list the total mass of the cluster, but give the masses of two mass concentrations instead. The masses are obtained from NFW fits to the data. Adding the masses yields a value of $M_{200} = 5.7 \pm 1.3 \times 10^{14} h^{-1} M_{\odot}$. Our data imply a significantly higher mass of $M_{200} = 15^{+5}_{-4} \times 10^{14} h^{-1} M_{\odot}$. By considering only two clumps, Kneib et al. (2003) might have underestimated the mass, as a more diffuse mass distribution would not have been accounted for. To avoid this problem we also fitted a SIS model to the tangential distortion presented in Figure 7 of Kneib et al. (2003). This yields an Einstein radius of $r_E \sim 18''$. Kneib et al. (2003) use sources with $23 < I < 26$, which yields a value of $\beta = 0.54$. Hence their signal corresponds to a velocity dispersion of 1075 km/s, which is in excellent agreement with our findings.

In summary, the agreement between our measurements and the literature values is fair, but there are a number of cases where the results are discrepant without a clear cause. However, based on the excellent quality of the CFH12k data used here, the fact that our weak lensing technique is well tested, and the comparison with other mass estimators (see following sections), we are confident that our results are robust and accurate.

Table 4. X-ray and dynamical properties

(1) name	(2) L_x [$10^{44} h^{-2} \text{erg/s}$]	(3) kT_x [keV]	(4) σ_{dyn} [km/s]	(5) ref.
A2390	30.5	9.2 ± 0.6	1262^{+89}_{-68}	1
MS 0016+16	39.3	$8.7^{+0.8}_{-0.7}$	1127^{+166}_{-112}	1
MS 0906+11	6.65	6.1 ± 0.4	886^{+78}_{-68}	1
MS 1224+20	3.3	$4.8^{+1.2}_{-1.0}$	831^{+129}_{-57}	1
MS 1231+15	—	—	686^{+65}_{-50}	1
MS 1358+62	9.3	$6.7^{+0.6}_{-0.5}$	1003^{+61}_{-52}	1
MS 1455+22	12.7	4.5 ± 0.2	1032^{+130}_{-95}	1
MS 1512+36	4.1	$3.6^{+0.9}_{-0.7}$	575^{+138}_{-90}	1
MS 1621+26	8.1	$6.5^{1.3}_{-1.0}$	839^{+67}_{-53}	1
A68	11.3	$8.0^{+0.8}_{-0.6}$	—	
A209	—	—	—	
A267	8.6	$5.9^{+0.5}_{-0.4}$	—	
A383	—	—	—	
A963	9.4	6.6 ± 0.4	—	
A1689	25.1	$9.2^{+0.4}_{-0.3}$	1172^{+123}_{-99}	2
A1763	15.6	$7.7^{+0.5}_{-0.4}$	—	
A2218	8.3	$7.0^{+0.4}_{-0.3}$	1222^{+147}_{-109}	2
A2219	32.8	$9.8^{+0.7}_{-0.6}$	—	
A370	13.4	7.2 ± 0.8	859^{+118}_{-112}	2
CL0024+16	3.5	$5.2^{+2.0}_{-1.3}$	911^{+81}_{-107}	2

Column 1: cluster name; Column 2: Bolometric X-ray luminosity from Horner (2001). The values listed here are corrected for galactic absorption, and transformed to the cosmology adopted in this paper. Column 3: X-ray temperature from Horner (2001) based on ASCA observations. The errors indicate the 90% confidence intervals. Column 4: velocity dispersion of cluster galaxies; Column 5: references for velocity dispersions. (1) Borgani et al. (1999); (2) Girardi & Mezzetti (2001)

4.2 Comparison with dynamical mass estimates

The measurement of the line-of-sight velocity dispersion clearly benefits from observing a large number of galaxies. Such observations decrease the statistical error, but also allow for a better rejection of interlopers and for the identification of substructures. These studies are time consuming, and as a result only a relatively small number of clusters have been studied in sufficient detail.

The clusters studied in this paper are well studied clusters and therefore have relatively good spectroscopic coverage. Nine of the clusters are part of the CNOC1 redshift survey sample (e.g., Carlberg et al., 1996; Yee et al., 1996). Borgani et al. (1999) (re-)derived velocity dispersions for the clusters in this sample using an interloper rejection scheme which is more sophisticated than the one used by Carlberg et al. (1996), which also enabled them to measure separate velocity dispersions for the two clusters in the field of MS0906. The velocity dispersions derived by Borgani et al. (1999) are listed in Column 4 of Table 4. The dynamical data for the remaining clusters in our sample are also listed in Table 4.

Figure 5 shows the velocity dispersion of the cluster galaxies versus the weak lensing estimate using the SIS fit to the data. The solid points correspond to the clusters in the CNOC1 sample. The agreement between the weak lens-

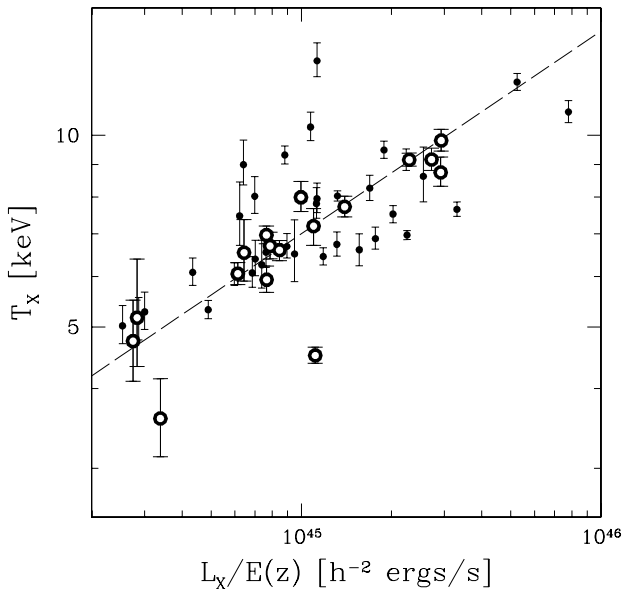


Figure 6. Plot of the ASCA temperature from Horner (2001) as a function of bolometric X-ray luminosity. The large open points correspond to the clusters studied in this paper. The small points indicate the clusters proposed as part of the Canadian Cluster Comparison Project. Thirty of these have been observed using Megacam on CFHT. Note the tight $L-T$ relation for the clusters studied in this paper, which does not appear to be representative of the full population of galaxy clusters studied as part of CCCP.

ing and dynamical measurements is excellent for these data. The open points correspond to measurements from Girardi & Mezzetti (2001), which also agree with the lensing estimates, albeit with a larger scatter. Compared to the CNOC1 sample, these four clusters show evidence of more complicated dynamics.

4.3 Comparison with X-ray properties

Much work has been devoted to the X-ray properties of galaxy clusters. In particular scaling relations between the X-ray luminosity, temperature and mass are of great interest as they provide clues about cluster formation. For instance, simple self-similar models (e.g., Kaiser 1986; Bryan & Norman 1998) predict power law relations between the mass, temperature and luminosity. More detailed numerical simulations (e.g., Evrard, Metzler & Navarro, 1996; Bryan & Norman, 1998) also provide evidence for simple scaling relations. If the gas is virialised, the mass M_Δ is given by

$$E(z)M_\Delta \propto T^{3/2} \quad (12)$$

where

$$E(z) = \frac{H(z)}{H_0} = \sqrt{\Omega_m(1+z)^3 + \Omega_\Lambda} \quad (13)$$

for flat cosmologies. The relevant temperature is the mean mass-weighted temperature within the radius r_Δ . As mentioned earlier, X-ray observations typically measure temperatures out to r_{2500} , which is the radius we will focus on.

The source of the X-ray emission is bremsstrahlung and therefore one expects that $L_X/E(z) \propto T^2$. The observed slope is found to be steeper (e.g., Edge & Stewart 1991; Markevitch, 1998; Arnaud & Evrard, 1999). For clusters with temperatures ≥ 2 keV the slope is ~ 3 , with even steeper slopes observed for lower temperature galaxy groups (e.g., Helsdon & Ponman 2000). Allen & Fabian (1998) have argued that the steeper slope, compared to the self-similar case, of the hotter clusters is caused by the effects of cool central components. But studies that attempt to account for this, still find steeper slopes, with values ~ 2.7 (e.g., Markevitch, 1998; Lumb et al. 2004).

When deriving X-ray temperatures, various groups employ different approaches to deal with temperature gradients and cool cores. To avoid introducing scatter caused by variations in the analysis method, we use the results from Horner (2001). The temperatures are based on ASCA observations. Although these measurements are not necessarily the most recent and accurate, they do provide a large sample, analysed homogeneously. As a caveat, we note that Horner (2001) did not attempt to correct for the cool centres of clusters. As part of the Canadian Cluster Comparison Project¹ (CCCP) we will derive X-ray properties in a consistent manner from modern Chandra and XMM observations, accounting for temperature variations.

The large open points in Figure 6 indicate the temperature as a function of bolometric luminosity for the clusters studied in this paper. With the exceptions of MS1455+22 and MS1512+36 (both strong ‘cooling flow’ clusters), the clusters follow a very tight relation. If we exclude these outliers, we find a slope of 3.57 ± 0.23 for our sample.

The aim of the CCCP is not only to derive X-ray temperatures in a consistent manner, but also involves the systematic study of the scatter in the relation between the weak lensing mass and the X-ray properties. This paper is a first attempt, but a more comprehensive study requires a larger sample of clusters. As part of the CCCP we therefore complement the sample studied here with an additional 30 massive clusters, resulting in a sample of ~ 50 clusters with $T > 5$ keV, with lensing masses derived from deep CFHT imaging.

The small points in Figure 6 correspond to the additional clusters in the CCCP sample. Although many of these clusters lie on the same relation as the clusters studied here, the overall scatter is significantly larger! Part of the scatter is likely to be caused by the fact that Horner (2001) did not correct for the presence of cool cores. For instance, Markevitch (1998) has shown that a considerable fraction of the scatter in the $L-T$ relation stems from scatter in the strength of the cool core. This is supported by theoretical models which indicate that a cool core lowers the average temperature and raises the X-ray luminosity of a cluster of a given mass (e.g., Voit et al. 2002; McCarthy et al. 2004). However, the sample of clusters studied here contains a typical mix of cooling and non-cooling flow systems similar to other studies (e.g., Peres et al. 1998; Bauer et al. 2005) and thus we do not expect a bias towards the selection of clusters with relatively weak cool cores.

¹ <http://www.astro.uvic.ca/~hoekstra/CCCP.html>

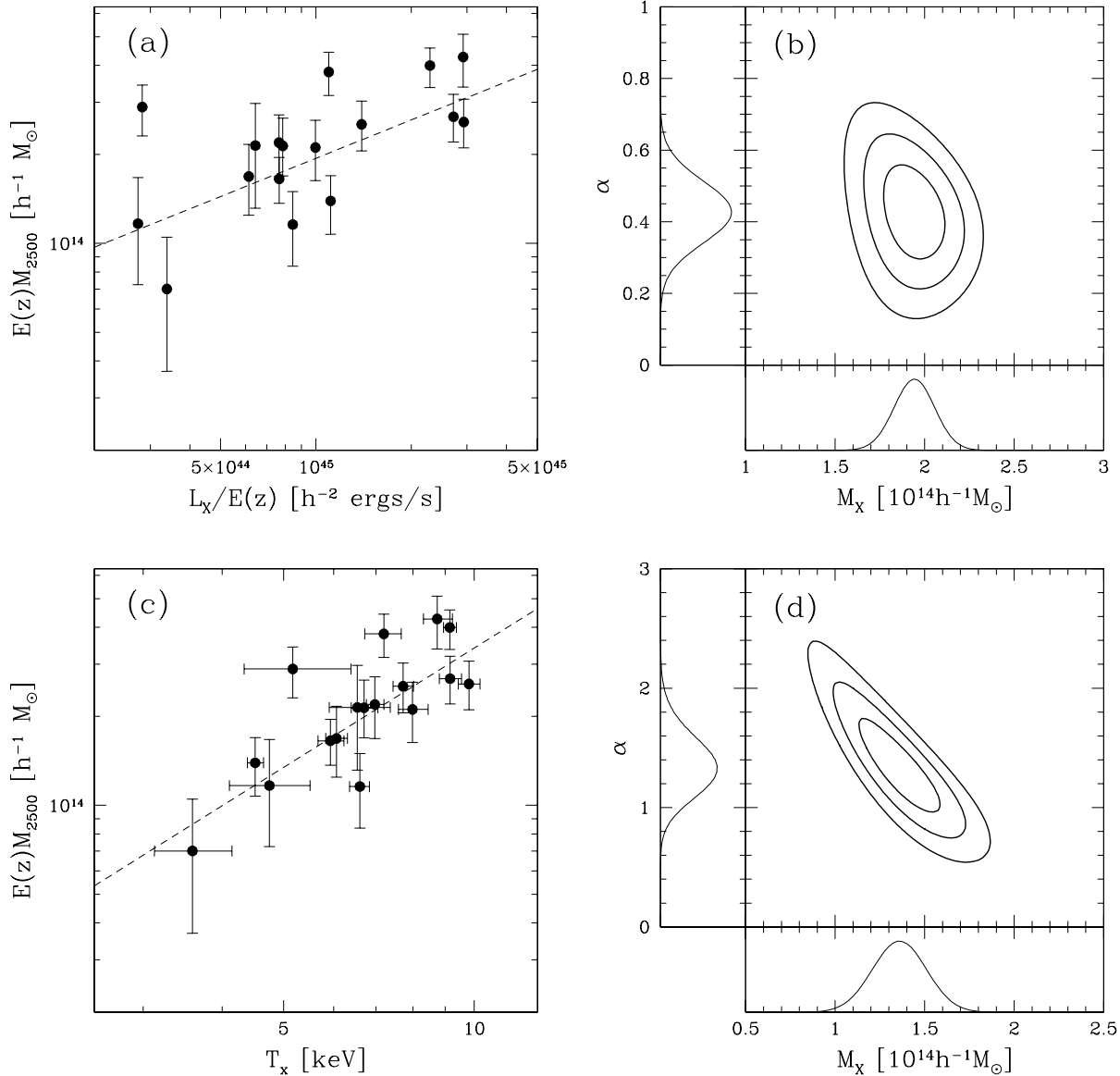


Figure 7. Panel (a): M_{2500} as a function of the bolometric X-ray luminosity. To account for the range in redshift of the clusters, the mass and luminosity have been rescaled using the corresponding value for $E(z)$. Panel (b): M_{2500} as a function of the X-ray temperature. The dashed lines indicate the best fit power law relations. Panel (a): Likelihood contours for the slope of the $M_{2500} - L_X$ relation and the mass of a cluster with a luminosity of $L_X = 10^{45}$ ergs/s at $z = 0$. Panel (b): Likelihood contours for the slope of the $M_{2500} - T_X$ relation and the mass of a cluster with a temperature of $T_X = 5$ keV at $z = 0$. The contours indicate the 68.3%, 95.4% and 99.7% confidence limits on two parameters jointly. The side panels show the probability density distribution for each parameter (while marginalising over the other).

Nevertheless, to understand the wide range of cluster properties, larger samples of well studied clusters are needed. Such samples will also improve our estimates of the normalisation and slope of the mass-temperature and mass-luminosity relations. The observed slopes of the mass-temperature relation agree well with theoretical predictions (e.g., Evrard et al. 1996). However, models that lack feedback processes do not fare so well for the amplitude. Compared to these models, X-ray observations find lower masses (e.g., Horner et al. 1999; Nevalainen et al., 2000; Reiprich & Böhringer, 2002; Arnaud et al. 2005). The origin of the

differences between theory and observations are not fully resolved, but several explanations have been proposed, many of which are related to non-gravitational physics. Cooling and feedback processes tend to alter the mass-temperature relation in a systematic way by raising the gas entropy level (as compared to the purely gravitational heating scenario). The net result is a increased temperature, or lower normalisation (e.g., Voit et al. 2002; Borgani et al. 2004). Because the X-ray mass estimates are also affected by the complex ICM physics, an independent weak lensing mass es-

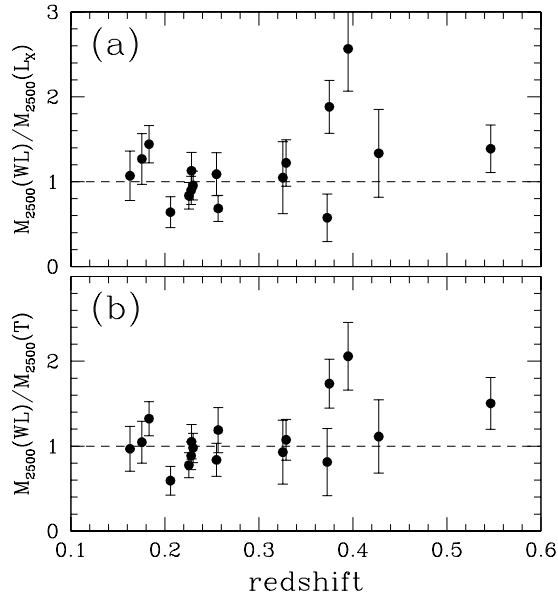


Figure 8. *Panel (a):* ratio of M_{2500} from the weak lensing analysis and the best fit mass-luminosity relation as a function of redshift. *Panel (b):* like a, but now for the best fit mass-temperature relation. The results suggest that the higher redshift clusters preferentially have larger than expected lensing masses, but a larger sample is required to make definite statements.

estimate is of great importance if we want to understand the mass-temperature relation.

Using the expected relation between luminosity and temperature, these simple models also predict that the mass and luminosity are related through

$$E(z)M_{\Delta} = \left(\frac{L_X}{E(z)} \right)^{3/4}. \quad (14)$$

Figure 7a shows the observed mass-luminosity relation. We use the value for M_{2500} derived from the aperture mass method. The best fit power law model is indicated by the dashed line. Figure 7b shows the likelihood contours for the parameters of this power law model for the M_{2500} –luminosity relation. The best fit model has a $\chi^2 = 38.1$ for 15 degrees of freedom. Hence the mass-luminosity shows evidence of intrinsic scatter. We find a slope of $\alpha = 0.43^{+0.09}_{-0.10}$ and a mass of $M_{2500} = 1.94^{+0.11}_{-0.12} \times 10^{14} h^{-1} M_{\odot}$ for a cluster with a luminosity of $10^{45} h^{-2} \text{ergs/s}$. The slope expected from simple self-similar models is ruled out by our measurements at the $\sim 3\sigma$ level. This is not surprising, as this reflects the fact that the observed $L - T$ relation is steeper than the one expected from self-similar models: if we assume $M \propto T^{3/2}$ and $L \propto T^3$, we expect $M \propto L^{1/2}$, as is observed.

Figure 7c shows the observed mass-temperature relation. We find $\chi^2 = 25.3$ for the best fit power law model, which is somewhat high, but significantly smaller than for the mass-luminosity relation. The likelihood contours for the power law model parameters are presented in Figure 7d. In this case we find a slope $\alpha = 1.34^{+0.30}_{-0.28}$, which agrees well with the self-similar slope of 1.5. The slope also agrees well

with studies based on X-ray data alone (e.g., Nevalainen et al. 2000; Allen et al., 2001; Arnaud et al. 2005; Vikhlinin et al. 2006).

Our best fit power law model yields a mass of $M_{2500} = (1.4 \pm 0.2) \times 10^{14} h^{-1} M_{\odot}$ for a cluster with a temperature of 5 keV. Allen et al. (2001) list a mass of $M_{2500} = (3.8 \pm 0.4) \times 10^{14} h^{-1} M_{\odot}$ for a 10 keV cluster (assuming a slope of 1.5). If we fix the slope to 1.5, we find $M_{2500} = (3.6 \pm 0.2) \times 10^{14} h^{-1} M_{\odot}$ for a 10 keV cluster, which is in excellent agreement with Allen et al. (2001).

Arnaud et al. (2005) studied the M-T relation of a sample of 6 nearby relaxed clusters ($T > 3.5$ keV), using XMM-Newton. They find a mass of $(1.3 \pm 0.04) \times 10^{14} h^{-1} M_{\odot}$ for a 5 keV cluster, in excellent agreement with our findings. Finally, Vikhlinin et al. (2006) list a mass of $(0.9 \pm 0.05) \times 10^{14} h^{-1} M_{\odot}$ for a 5 keV cluster. This result is marginally consistent with our result. Note, however, that the ASCA temperatures used here may be biased low, because they have not been corrected for cool cores. A rough comparison between the Vikhlinin et al. (2006) and Horner (2001) temperatures suggest that the ASCA temperatures used here are about 10% lower. This suggests that our normalisation may need to be reduced by about 15%.

So far, we have assumed that the evolution of the X-ray properties follows the expected evolution, parameterized by $E(z)$. To examine whether the cluster properties show evidence of additional evolution, we plot the ratio of the lensing mass and the best mass from the best fit $M - L_X$ relation in Figure 8a. Similarly, Figure 8b shows the results for the $M - T$ relation. The clusters with $z > 0.35$ seem to have somewhat larger than expected lensing masses, but a larger sample is required to confirm this suggestion.

We find that the residuals in the $M - L_X$ and $M - T$ relation are highly correlated. This is not too surprising, given that the clusters in our sample follow such a tight $L - T$ relation. The implications, however, are interesting. The largest outliers in Figure 8 are CL0024+16 and A370, for which we find lensing masses that are ~ 2 times larger than expected from the X-ray properties. Yet, these clusters lie on the $L - T$ relation. This discrepancy could indicate a problem with the weak lensing mass determination, but we were unable to identify an obvious measurement error. However, these clusters have been studied in detail because of their extreme strong lensing properties. Therefore, these clusters may be considered “lensing-selected”, which could explain their larger than expected masses when compared to their X-ray properties. A related observation is that both clusters show evidence of recent, or ongoing merging. The kinematics of CL0024+16 have been studied in detail by Czoske et al. (2002), who conclude that it might have experienced a high speed collision. A370 consists of two distinct mass concentrations (e.g., Kneib et al., 1993), which enhances its strong lensing cross-section.

5 CONCLUSIONS

Tremendous progress in measurement techniques, in conjunction with new field imaging capabilities on large telescopes has led to the next step in the study of galaxy clusters using weak gravitational lensing: the study of the mass distribution of large samples of clusters. This paper presents

the first results of such a systematic, multiwavelength study of rich clusters of galaxies.

In this paper we have presented new measurements of the masses of 20 X-ray luminous clusters of galaxies at intermediate redshifts. The results are based on a careful analysis of deep archival *R*-band data obtained using the Canada-France-Hawaii-Telescope. In particular, we accounted for a number of subtle effects that, if ignored, can lead to small biases or incorrect error estimates. Thanks to the wide field of view of the CFH12k camera, we were able to derive masses that are essentially model independent

Comparison of the lensing results with measurements of the velocity dispersion of cluster galaxies shows good agreement. We typically find good agreement between our results and weak lensing mass estimates in the literature. Assuming a power law between the lensing mass and the X-ray temperature, $M_{2500} \propto T^\alpha$, we find a best fit slope of $\alpha = 1.34^{+0.30}_{-0.28}$. This slope agrees with self-similar cluster models and studies based on X-ray data alone (Nevalainen et al. 2000; Allen et al. 2001; Arnaud et al. 2005; Vikhlinin et al. 2006). For a cluster with a temperature of $kT = 5$ keV we obtain a mass $M_{2500} = (1.4 \pm 0.2) \times 10^{14} h^{-1} M_\odot$, in fair agreement with recent Chandra and XMM studies (e.g., Allen et al. 2001; Arnaud et al. 2005; Vikhlinin et al. 2006).

The comparison to X-ray properties is complicated by the fact that the analysis pipelines employed by different groups can yield quite different luminosities and temperatures. We therefore used measurements by Horner (2001) which are based on ASCA observations and not corrected for the presence of cool cores. As part of the Canadian Cluster Comparison Project, we are re-analysing available modern X-ray data in a consistent manner. Furthermore, to improve constraints on the normalisation and slope of the scaling relations between mass and X-ray properties, as well as quantifying the scatter in these relations, even larger samples of clusters, with accurate weak lensing masses, are required. To achieve this goal, we have recently augmented the sample of clusters studied in this paper with deep g' and r' CFHT Megacam imaging of an additional 30 massive clusters.

We thank Andisheh Mahdavi and Arif Babul for many useful discussions. We are also grateful to Pat Henry and Mark Voit for comments on the manuscript. This research was supported by the National Science and Engineering Research Council (NSERC), the Canadian Foundation for Innovation (CFI), and the Canadian Institute for Advanced Research (CIAR). This research used the facilities of the Canadian Astronomy Data Centre operated by the National Research Council of Canada with the support of the Canadian Space Agency.

REFERENCES

- Allen, S.W. 1998, MNRAS, 296, 392
 Allen, S.W. & Fabian, A.C. 1998, MNRAS, 297, L63
 Allen, S. W., Schmidt, R.W. & Fabian, A.C. 2001, MNRAS, 328, L37
 Allen, S.W., Schmidt, R.W., Ebeling, H., Fabian, A.C. & van Speybroeck, L. 2004, MNRAS, 353, 457
 Arnaud, M., Pointecouteau, E. & Pratt, G.W. 2005, A&A, 411, 893
 Arnaud, M. & Evrard, A.E. 1999, MNRAS, 305, 631
 Bardeau, S., Kneib, J.-P., Czoske, O., Soucail, G., Smail, I., Ebeling, H., Smith, G.P. 2005, A&A, 434, 433
 Bartelmann, M. 1996, A&A, 313, 697
 Bauer, F.E., Fabian, A.C., Sanders, J.S., Allen, S.W. & Johnstone, R.M. 2005, MNRAS, 359, 1481
 Bertin, E. & Arnouts, S. 2006, A&AS, 117, 393
 Borgani, S., Girardi, M., Carlberg, R.G., Yee H.K.C. & Ellingson, E. 1999, ApJ, 527, 561
 Borgani, S., Murante, G., Springel, V., Diaferio, A., Dolag, K., Moscardini, L., Tormen, G., Tornatore, L. & Tozzi, P. 2004, MNRAS, 348, 1078
 Bryan, G.L. & Norman, M.L. 1998, ApJ, 495, 80
 Bullock, J.S. et al. 2001, MNRAS, 321, 559
 Carlberg, R.G., Yee, H.K.C., Ellingson, E., Abraham, R., Gravel, P., Morris, S., & Pritchet, C.J. 1996, ApJ, 462, 32
 Corless, V. & King, L. 2006, MNRAS, submitted, astro-ph/0611193
 Clowe, D., Luppino, G.A., Kaiser, N., Henry, J.P., & Gioia, I.M. 1998, ApJ, 497, L61
 Clowe, D. & Schneider, P. 2001, A&A, 379, 384
 Cypriano, E.S., Sodre, Jr., L., Kneib, J.-P., Campusano, L.E. 2004, ApJ, 613, 95
 Dahle, H., Kaiser, N., Irgen, R.J., Lilje, P.B., & Maddox, S. 2002, ApJS, 139, 313
 Dubinski, J. & Carlberg, R.G. 1991, ApJ, 378, 496
 Ebeling, H., Voges, W., Böhringer, H., Edge, A.C., Huchra, J.P. & Briel, U.G., 1996, MNRAS, 281, 799
 Edge, A.C. & Stewart, G.C. 1991, MNRAS, 252, 414
 Eke, V.R., Cole, S. Frenk, C.S., & Henry, J.P. 1998, MNRAS, 298, 1145
 Evrard, A.E. 1989, ApJ, 341, 71
 Evrard, A.E., Metzler, C.A. & Navarro, J.F. 1996, ApJ, 469, 494
 Fahlman, G., Kaiser, N., Squires, G., & Woods, D. 1994, ApJ, 431, L71
 Fernández-Soto, A., Lanzetta, K.M., & Yahil, A. 1999, ApJ, 513, 34
 Fischer, P. 1999, AJ, 117, 2024
 Gioia, I., Maccacaro, T., Schild, R.E., Wolter, A., Stocke, J.T., Morris, S.L. & Henry, J.P. 1990, ApJS, 72, 567
 Girardi, M., & Mezzetti, M. 2001, ApJ, 548, 79
 Gorenstein, M.V., Shapiro, I.L., & Falco, E.E. 1988, ApJ, 327, 693
 Haiman, Z., Mohr, J.J. & Holder, G.P. 2001, ApJ, 553, 545
 Helsdon, S.F. & Ponman, T.J. 2000, MNRAS, 315, 356
 Henry, J.P. 2000, ApJ, 534, 565
 Heymans, C. et al. 2006, MNRAS, 368, 1323
 Hoekstra, H., Franx, M., Kuijken, K., & Squires, G. 1998, ApJ, 504, 636
 Hoekstra, H., Franx, M., Kuijken, K. 2000, ApJ, 532, 88
 Hoekstra, H. 2001, A&A, 370, 743
 Hoekstra, H., Yee, H.K.C., & Gladders, M. 2002a, NewAR, 46, 767
 Hoekstra, H., Yee, H.K.C., & Gladders, M. 2002b, ApJ, 577, 595
 Hoekstra, H. 2003, MNRAS, 339, 1155
 Hoekstra, H., Mellier, Y., van Waerbeke, L., Semboloni, E., Fu, L., Hudson, M.J., Parker, L.C., Tereno, I., & Benabed, K. 2006, ApJ, 647, 116
 Horner, D.J. 2001, PhD thesis, University of Maryland
 Horner, D.J., Mushotzky, R.F. & Scharf, C.A. 1999, ApJ, 520, 78
 Kaiser, N. 1986, MNRAS, 222, 323
 Kaiser, N., Squires, G., & Broadhurst, T. 1995, ApJ, 449, 460
 Kneib, J. P., Mellier, Y., Fort, B. & Mathez, G. 1993, A&A, 273, 367
 Kneib, J.-P., et al. 2003, ApJ, 598, 804
 Levine, E.S., Schultz, A.E., & White, M. 2002, ApJ, 577, 569
 Limousin, M. et al. 2006, astro-ph/0612165
 Lumb, D.H. et al. 2004, A&A, 420, 853
 Luppino, G.A., Kaiser, N. 1997, ApJ, 475, 20
 Markevitch, M. 1998, ApJ, 504, 27

- McCarthy, I., Balogh, M.L., Babul, A., Poole, G.B., & Horner, D.J. 2004, *ApJ*, 613, 811
- Metzler, C.A., White, M., Norman, M., & Loken, C. 1999, *ApJ*, 520, L9
- Metzler, C.A., White, M., & Loken 2001, *ApJ*, 547, 560
- Miralda-Escude, J. 1991, *ApJ*, 370, 1
- Moore, B., Quinn, T., Governato, F., Stadel, J., & Lake, G. 1999, *MNRAS*, 310, 1147
- Navarro, J.F., Frenk, C.S., & White, S.D.M. 1995, *MNRAS*, 275, 56
- Navarro, J.F., Frenk, C.S., & White, S.D.M. 1997, *ApJ*, 490, 493
- Nevalainen, J., Markevitch, M., & Forman, W. 2000, *ApJ*, 532, 694
- Peres, C.B., Fabian, A.C., Edge, A.C., Allen, S.W., Johnstone, R.M. & White, D.A. 1998, *MNRAS*, 298, 416
- Reiprich, T.H. & Böhringer, H. 2002, *ApJ*, 567, 716
- Schneider, P. 2005, Lecture Notes of the 33rd Saas-Fee Advanced Course, G. Meylan, P. Jetzer & P. North (eds.), Springer-Verlag: Berlin, p.273, astro-ph/0509252
- Smith, G., Kneib, J.-P., Smail, I., Mazzotta, P., Ebeling, H. & Czoske, O. 2005, *MNRAS*, 359, 417
- Squires, G., Kaiser, N., Fahlman, G., Babul, A., & Woods, D. 1996a, *ApJ*, 469, 73
- Squires, G., Kaiser, N., Babul, A., Fahlman, G., Woods, D. Neumann, D.M., & Boehringer, H. 1996b, *ApJ*, 461, 572
- Taylor, A.N., Bacon, D.J., Gray, M.E., Wolf, C., Meisenheimer, K., Dye, S., Borch, A., Kleinheinrich, M., Kovacs, Z. & Wisotzki, L. 2004, *MNRAS*, 353, 1176
- Tyson, J.A., Wenk, R.A., & Valdes, F. 1990, *ApJ*, 349, L1
- Voit, G.M., Bryan, G.L., Balogh, M.L., & Bower, R.G. 2002, *ApJ*, 576, 601
- van Waerbeke, L., Mellier, Y. & Hoekstra, H. 2005, *A&A* 429, 75
- Vikhlinin, A., VanSpeybroeck, L., Markevitch, M., Forman, W.R., & Grego, L. 2002, *ApJ*, 578, L107
- Vikhlinin, A., Kravtsov, A., Forman, W., Jones, C., Markevitch, M., Murray, S. S., Van Speybroeck, L. 2006, *ApJ*, 640, 691
- Wolf, C. et al. 2004, *A&A*, 421, 913
- White, M., van Waerbeke, L. & Mackey, J. 2002, *ApJ*, 575, 640
- Wright, C.O. & Brainerd, T.G. 2000, *ApJ*, 534, 34
- Yee, H.K.C., Ellingson, E., & Carlberg, R.G. 1996, *ApJS*, 102, 269